Numerical investigation of aerodynamic responses and wake characteristics of a floating offshore wind turbine under atmospheric boundary layer inflows

Shun Xu [a], Tiegang Zhuang [b], Weiwen Zhao [a], Decheng Wan [a],*

[a] *Computational Marine Hydrodynamics Lab (CMHL), School of Naval Architecture, Ocean and Civil Engineering, Shanghai Jiao Tong University, Shanghai, China*
[b] *Key Laboratory of Far-shore Wind Power Technology of Zhejiang Province, Huadong Engineering Corporation Limited, Hangzhou, China*

ABSTRACT

The atmospheric boundary layer (ABL) inflow has significant effects on behaviors of floating offshore wind turbine (FOWT), especially for large-size wind turbine. In this study, numerical investigation of aerodynamics and wakes of a semi-submersible FOWT under ABL inflow is performed. The quasi-equilibrium ABL wind field is generated by large eddy simulations (LES) with sufficient simulation duration. The FOWT wakes are modeled by incorporating LES and actuator line model (ALM) in the computational fluid dynamics (CFD) framework, and the FOWT dynamic responses are simulated by FAST code. A two-way coupling procedure is employed, in which the wind velocity around wind turbine sampled in CFD framework and the wind turbine's body forces and positions solved by FAST code are delivered to each other. The simulation case of a bottom-fixed wind turbine is performed to provide some comparable data. It is revealed that the power variation of FOWT is dominated by atmospheric turbulence, more than platform motions. The slightly enhanced out-of-plane shear force and bending moment of FOWT are caused by platform motions. Owing to the entrance of ambient atmospheric flow into wind turbine wakes, significant deflection of wakes is visualized. In addition, the wake center of FOWT is far away from hub height level due to pitch motion of platform, which is a potential benefit factor for downstream wind turbines. The spatiotemporal characteristics of turbulence intensity in FOWT wakes are complex, and the discrepancies of wakes between floating and bottom-fixed scenarios are not significant.

1. Introduction

The floating offshore wind turbine (FOWT) has become a hot topic over the past few decades. For the design of FOWT, accurate prediction of its dynamic responses (i.e., aerodynamic performance, hydrodynamic responses and mooring tension) is one of the challenges. However, due to the coupling characteristics between components of the FOWT, as well as the complex atmospheric inflow and extreme sea conditions, accurate prediction of dynamic responses of FOWT needs further investigations. In order to systematically investigate the dynamic responses of FOWT under realistic environment conditions, as well as to evaluate the design reliability, some FOWT prototypes have been designed and installed. For instance, the Hywind Demo 2.3 MW FOWT (Skaare et al., 2015), the WindFloat 2 MW FOWT (Roddier et al., 2010) and the 1:8 scale prototype of 6 MW FOWT called VolturnUS (Viselli et al., 2016), etc. Although those FOWT prototypes are operated under

real environmental conditions and can reflect the most realistic mechanism, it is hard and unrealistic to assess their behaviors under specified environment conditions. Specifically, waiting for typhoon to investigate the FOWT's performance and safety under extreme sea conditions may cost a few years or more. In contrast to the FOWT prototypes, experiments of scale-down FOWT model have the ability to guarantee desired incident wind and wave conditions. Therefore, the scale-down experiments have been widely conducted to study dynamic responses of FOWT (Amaral et al., 2021; Gueydon et al., 2021; Li et al., 2018a). Although the experimental works exhibit some interesting results, the Froude and Reynolds number scaling laws cannot be simultaneously guaranteed (Otter et al., 2022).

In recent years, with the aim of avoiding limitations of prototypes and model experiments, the numerical methods have been proposed to study dynamic responses of FOWT. Lots of analysis codes have been developed and employed to predict the fully-coupled aero-hydro-moor-

servo dynamics of FOWT, such as FAST, 3Dfloat, Bladed and HAWC2 (Atcheson et al., 2016; Jonkman and Buhl, 2005; Nygaard et al., 2016; Robertson et al., 2014a). The aerodynamic force calculated by those codes almost all use blade element momentum (BEM) theory, which is a commonly used method in real-world engineering field. In order to pursue more accurate results, correction models are introduced into the BEM based on the experience of researchers (Madsen et al., 2010). Additionally, Matha et al. (2011) pointed out that the inflow wind conditions of FOWT are more sophisticated, compared to that of bottom-fixed wind turbine (BFWT). This indicates that the application of BEM method on the predictions of aerodynamic loads of FOWT needs further investigations (Sebastian and Lackner, 2013).

Owing to the significant development of high-performance computers, computational fluid dynamics (CFD) models have been proposed for studying dynamic responses of FOWT. By incorporating the STAR-CCM + and developed in-house code, Tran et al. (Tran and Kim, 2016a) proposed a aero-hydrodynamic numerical framework for FOWT. The overset mesh technique is employed to address large movements of FOWT. The dynamic responses of FOWT are comprehensively validated, including unsteady aerodynamics, platform hydrodynamics and aero-hydrodynamic responses. However, it should be mentioned that the fully resolved CFD simulations of FOWT are computationally unaffordable. Troldborg et al. (2007) noted that the actuator line model (ALM) can reduce the computational costs by representing wind turbine blades with virtual actuator lines, while the desirable results are guaranteed by solving the Navier-Stokes equations of flow field. Consequently, the unsteady ALM (UALM) was proposed for the aerodynamics of FOWT by considering an additional velocity caused by platform motions (Huang et al., 2019, 2021, 2022; Li et al., 2015; Huang and Wan, 2019a). Cheng et al. (2019) studied the dynamic characteristics of a semi-submersible FOWT based on the UALM method. Besides, Huang and Wan (2019b) explored the aero-hydrodynamic interactions of a spar FOWT under various platform motion modes and wind turbine states.

As the size of FOWT increases with aim of increasing captured wind energy and decreasing levelized cost of energy, the effect of atmospheric boundary layer (ABL) with high turbulence and non-stationary (Porté-Agel et al., 2020) on dynamic responses of FOWT becomes more significant. Therefore, a realistic representation of ABL inflow is critical for the design of FOWT. Two turbulence models are recommended by the International Electrotechnical Commission (IEC) standard for simulations of ABL wind field, the Mann spectral tensor model (Mann, 1994) and the Kaimal spectral and exponential coherence model (Kaimal et al., 1972), hereafter referred to as "Mann model" and "Kaimal model", respectively. Li et al. (2018b) investigated the influences of ABL wind field generated by Kaimal model on aerodynamics of a FOWT. Their findings indicated that the power generation is sensitive to the ABL wind field. Putri et al. (2020) drew an interesting conclusion that the lower wind lateral coherence of Mann model results in significant increase of tower base side-side bending moment and tower top torsional moment, in comparison with that of Kaimal model.

Large eddy simulations (LES) are employed in recent years to generated more realistic ABL wind fields. Compared to the LES and offshore measurements, generation of ABL wind fields using the Mann and Kaimal models exhibits a significant discrepancy for the spatio-temporal distribution of coherence (Nybø et al., 2020). Doubrawa et al. (2019) pointed out that the Kaimal model matches the high-fidelity LES wind field more closely than the Mann model at higher wind speeds, whereas the opposite is true at lower wind speeds. They also emphasized that the fatigue loads of a FOWT predicted by the two models are overpredicted in higher wind speed situations and underpredicted in lower wind speed cases. Some studies found that the fatigue life of mooring cables of a spar type FOWT estimated by Kaimal model is twice that of Mann model (Eliassen and Obhrai, 2016; Godvik, 2016). In addition, by applying more realistic models, the LES and a method using wind measurements from offshore site, the Mann model and Kaimal model have been proved that may lead to inaccurate predictions for the dynamic responses of FOWT (Nybø et al., 2022). Consequently, systematic studies should be performed to further evaluate the ability of the two models for generating the realistic ABL wind fields (Meneveau, 2019).

For the studies of wind turbine subjected to ABL wind field simulated by LES, the relevant studies for BFWT are more common compared to those of FOWT. Lu and Porté-Agel (2011) investigated the wake characteristics of a wind turbine subjected to the ABL wind field in neutral state. Due to the collective effects of turbulent inflow, Coriolis force and rotating turbine blades, asymmetry of wind turbine wakes were observed. Ning and Wan (2019) studied the wake meandering effect, which was caused by large-scale atmospheric turbulence and has significant effects on the operation performance of downstream wind turbine. Similarity, Churchfield et al. (2012a) examined the influence of atmospheric inflow and wind turbine wakes on the dynamic responses of wind turbine. It is shown that the loads on wind turbine caused by atmospheric inflow are as significant as that of upstream wind turbine wakes. In addition, Lee et al. (2012) noted that the effects of atmospheric stratification on the fatigue loads of wind turbine are significant. The platform motion is not considered in above studies, however, it can change the inflow condition of FOWT and has significant effects on wind turbine aerodynamics and wakes (Xu et al., 2022). The numerical results from Tran and Kim (2016b) showed that the gap distances among blade-up vortex tubes is variable due to contributions of platform surge motion and strong vortex-wake interactions. Huang et al. (Huang and Wan, 2019b) pointed out that the platform pitch motion has significant impacts on local relative wind speed of rotating blades, and wake deflection phenomenon is clearly observed in near wake region when platform pitch motion is considered. Zhang and Kim (2018) studied the aerodynamics for both FOWT and BFWT, and they found the rotor thrust of FOWT is increased by 7.8% compared to that of fixed scenario, whereas the rotor power is decreased by 10%. Johlas et al. (2019) investigated the wakes of a spar buoy FOWT immersed in ABL wind field and compared the results with those of fixed scenario. The differences in wake shape between floating and fixed cases are related to mean platform displacements, while the differences in wake turbulence are related to time-varying platform motion. After that, they conducted an investigation for the impacts of floating platform types on FOWT wakes (Johlas et al., 2020). It was discovered that the wakes of FOWT are deflected upwards compared to fixed wind turbine wakes, and spar wake deflects upwards more than the semi-submersible.

In this study, we perform numerical simulations to investigated the differences of wind turbine aerodynamics and wakes between FOWT and BFWT immersed in the ABL wind field simulated by LES. The precursor-successor simulation strategy is employed, in which the LES with sufficient simulation duration is employed to generate the quasi-equilibrium ABL wind field. Subsequently, the ABL wind field is introduced into successor stage that the wind turbine wakes and fully-coupled dynamics are simulated. The wind turbine wakes are modeled by the LES framework incorporated with the ALM, and the fully-coupled dynamics are solved using the FAST code.

The remainder of this study is organized as follows. In Section 2, the numerical methods composing of governing equations, aerodynamic modeling and simulation procedure are presented. The employed FOWT model, the computational setup for generation of ABL wind field, simulation of the wind turbine and wind-wave conditions are illustrated in Section 3. In Section 4, the numerical validation of aerodynamic performance of BFWT and platform motions of FOWT are presented, as well as the simulated ABL wind field. We present numerical results with some discussions in Section 5, and the main conclusions are summarized in Section 6.

2. Numerical methods

2.1. Governing equations

The LES technology is adopted to solve the spatial filtered continuity equation, momentum equation:

$$\frac{\partial \overline{u}_i}{\partial x_i} = 0 \tag{1}$$

$$\frac{\partial \overline{u}_i}{\partial t} + \frac{\partial}{\partial x_j}\left(\overline{u}_j \overline{u}_i\right) = \underbrace{-\frac{\partial \widehat{p}}{\partial x_i}}_{I} \underbrace{-\frac{1}{\rho_0}\frac{\partial}{\partial x_i}\overline{p}_0(x,y)}_{II} \underbrace{-2\varepsilon_{i3k}\Omega_3 \overline{u}_k}_{III} \underbrace{-\frac{\partial}{\partial x_j}\left(\tau_{ij}^D\right)}_{IV} + \underbrace{\frac{1}{\rho_0}f_i^T}_{V} \tag{2}$$

where the overbar denotes the spatial filtered value. $\overline{u}_i$ is the instantaneous spatial filtered velocity vector in three directions (i = 1, 2, 3 denote the streamwise (x-axis), spanwise (y-axis) and vertical (z-axis) directions). For the filtered momentum conservation equation, Term I is the gradient of modified pressure. Term II is the gradient of background pressure to drive fluid field move forward. Term III is the Coriolis force caused by earth rotation. Term IV is the divergence of deviatoric part of the fluid stress tensor. Note that the molecular viscous effect is not considered due to high Reynolds number of flow in ABL turbulence. Term V is the source term of body force of wind turbine, which is used to reflect the effects of wind turbine on flow field. More details about the governing equations can refer to (Churchfield et al., 2012a).

In the LES, the turbulence structures larger than the filter scale are directly captured and resolved, whereas the contribution of unresolved turbulence structures are modeled based on a subgrid-scale (SGS) model. The stress τ_{ij}^D is solved by a linear relationship:

$$\tau_{ij}^D = -2v^{SGS}\overline{S}_{ij} \tag{3}$$

where v^{SGS} is the SGS viscosity and calculated by the Smagorinsky model (Smagorinsky, 1963) and $\overline{S}_{ij}$ is the resolved strain-rate tensor, as shown in following equations:

$$\overline{S}_{ij} = \frac{1}{2}\left(\frac{\partial \overline{u}_i}{\partial x_j} + \frac{\partial \overline{u}_j}{\partial x_i}\right) \tag{4}$$

$$v^{SGS} = (C_s\Delta)^2\left(2\overline{S}_{ij}\overline{S}_{ij}\right)^{\frac{1}{2}} \tag{5}$$

where C_s is a model constant, here we set to 0.13. $\Delta = (\Delta_x\Delta_y\Delta_z)^{1/3}$ is the filter width, Δ_x, Δ_y and Δ_z are the local mesh lengths in x-, y- and z-directions, respectively.

2.2. Aerodynamic modelling

The ALM is employed to model the wind turbine blades, which was originally proposed by Sørensen and Shen (Sorensen and Shen, 2002). The basic idea behind the ALM is to represent wind turbine blades using rotating lines with body forces of two-dimensional blade elements along the radial direction. The body forces are determined by blade element theory, and subsequently, projected to the flow field to reflect the effects of wind turbine. Compared to the blade-resolved modeling, the computational costs are reduced by the ALM, while the accuracy of numerical results is guaranteed by using the CFD technique for solution of flow field. The body force of two-dimensional blade element is expressed by:

$$f = (L, D) = \frac{1}{2}\rho U_{rel}^2 cdr(C_L\vec{e}_L + C_D\vec{e}_D) \tag{6}$$

where L and D are the lift and drag forces, ρ denotes the air density, U_{rel} is the relative inflow wind velocity, c represents the chord length of two-dimensional blade element, dr is the width of blade element, C_L and C_D

denote the coefficients of lift and drag, which are determined by the local angle of attack, $\vec{e}_L$ and $\vec{e}_D$ are the unit vectors of lift and drag forces.

Fig. 1 shows the velocity vectors of the two-dimensional blade element. Compared to the original ALM for aerodynamic modeling of BFWT, the additional velocity U_M caused by platform motions is considered. The local attack angle α is determined by:

$$\alpha = \varphi - \beta, \varphi = tan^{-1}\left(\frac{U_z + U_{M,z}}{\Omega \times r + U_{M,\theta} - U_\theta}\right) \tag{7}$$

where φ denotes the local inflow angle, β represents the local pitch angle. U_z, U_θ are the axial and tangential components of inflow wind vector, $U_{M,z}$, $U_{M,\theta}$ are respectively the axial and tangential parts of additional velocity vector induced by platform motions. Ω is the rotor speed, r is the radial distance of the local two-dimensional blade element from rotor center. Once the local attack angle is determined, the body force is determined by the Equation (6).

As aforementioned, the source term of body force of wind turbine is added into momentum equation to reflect the distributions of wind turbine on flow field. The Gauss kernel function is employed, with the aim of avoiding numerical singularity and obtaining desired results. The body force after smoothing is as follows:

$$f_\varepsilon = f \otimes \eta_\varepsilon = \sum_{i=1}^{N} f_i(x_i, y_i, z_i, t)\frac{1}{\varepsilon^3\pi^{\frac{3}{2}}}exp\left[-\left(\frac{d_i}{\varepsilon}\right)^2\right] \tag{8}$$

where N is the number of body forces of wind turbine blades, (x_i, y_i, z_i) is the position of i-th body force, d_i denotes the distance between body force and projection position, ε is the projection width, here we set $\varepsilon \approx 2\Delta x$ as recommended by Troldborg (Troldborg et al., 2007), where Δx is the mesh scale near wind turbine blades.

2.3. Simulation procedure

The simulation procedure of FOWT subjected to the ABL wind field is illustrated in Fig. 2. Two numerical simulation stages are conducted, including a precursor stage for generation of ABL wind field and a successor stage for simulation of coupled behaviors of FOWT. More specifically, two steps of precursor stages are utilized. Step 1 is used to develop the quasi-equilibrium ABL flow field based on the LES with sufficient simulation duration. An additional continuity simulation, namely Step 2, is employed to save the time histories of inflow wind conditions for successor stage. In the successor stage, the FOWT is introduced into the ABL wind field, and the wakes and fully-coupled behaviors are conducted.

The generation of ABL wind field of precursor stage and the wake modeling of successor stage are performed in SOWFA (Churchfield et al., 2012b), which is a LES framework developed by National Renewable Energy Laboratory (NREL) based on the open source CFD framework
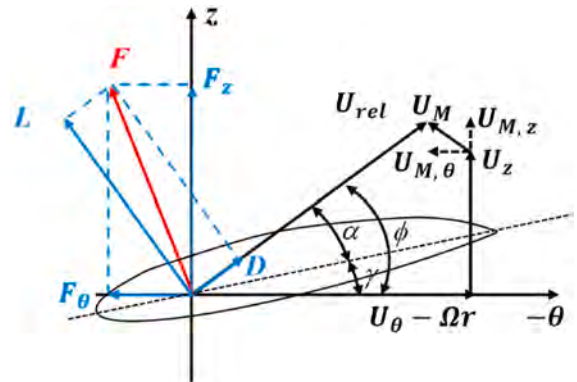

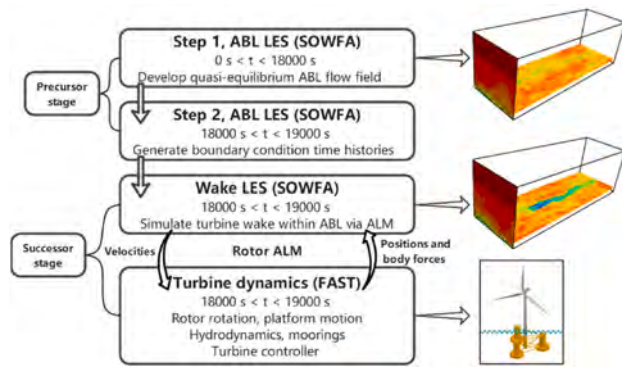Fig. 1. The velocity vectors of the two-dimensional blade element.

Fig. 2. The simulation procedure of FOWT subjected to the ABL wind field.

OpenFOAM (Greenshields, 2015) and applied for the simulations of large wind farm. The fully-coupled behaviors of FOWT under ABL inflow and incident wave are solved by FAST v8.16 (Jonkman and Buhl, 2005), which is an aero-hydro-servo simulation suite composed of AeroDyn for aerodynamic modeling, Elastodyn for structural dynamics, HydroDyn for time-domain hydrodynamics, InflowWind for one-way coupling with turbulence flow field, MoorDyn for mooring dynamics and ServoDyn for wind turbine control. Note that the two-way loose coupling between the FAST and the ALM is developed and proposed by SOWFA. Specifically, the flow field is resolved by incorporating LES and ALM, in which the inflow wind velocities are sampled along wind turbine blades and delivered to FAST. The fully-coupled dynamics of FOWT are simulated in FAST, and the body forces and positions of wind turbine are feedback to the LES framework for simulation of next time step. Note that the momentum part of blade element momentum theory for aerodynamics of FOWT is replaced by the ALM in the coupling procedure.

3. Computational set up

3.1. Floating wind turbine model

The semi-submersible FOWT of the Offshore Code Comparison Collaboration Continuation (OC4 Phase II) project (Coulling et al., 2013; Masciola et al., 2013; Robertson et al., 2014b) is adopted as the research object. The FOWT system includes the following three subsystems: the NREL 5 MW baseline wind turbine, the DeepCwind semi-submersible floating platform and the mooring system. The NREL 5 MW baseline wind turbine (Jonkman et al., 2009) is a conventional upwind turbine with three blades. The rated wind speed and rated power are 11.4 m/s and 5 MW, respectively. Table 1 shows the gross parameters of the wind turbine. In addition, a control system consisting of pitch controller and torque controller is incorporated to regulate the power output according to inflow wind speeds. Specifically, in above-rated wind speed scenarios, the blade pitch angle is increased by pitch controller to limit the power output. While in below-rated wind speed scenarios, the torque controller is active to maximize power generation by varying the rotor speed.

The OC4 semi-submersible floating platform is adopted to provide the buoyancy and support the wind turbine. The floating platform is composed of three offshore columns, one main column and several

pontoons, in which the offset columns present a triangle arrangement with the main column located at its center. Table 2 shows the gross parameters of OC4 semi-submersible floating platform. The draft of this floating platform is 20 m, and the top of this floating platform is 10 m above the sea water level (SWL). Total mass of the floating platform is 13,473,000 kg and mass center is 13.5 m below the SWL.

The mooring system including three mooring lines is used to limit the platform motions and guarantee the operational safety of FOWT system. The mooring lines are arranged symmetrically with 120° offset between adjacent lines. In this study, we set the mooring line 2 parallel to the direction of combined wind-wave, as well as aligned with the direction of platform surge motion. Table 3 exhibits the gross parameters of mooring system. The depth of anchors and fairleads are 200 m and 14 m, respectively.

3.2. Precursor stage

Differently from the stochastic turbulence generation method, such as TurbSim with the Mann and Kaimal models, the simulation strategy of precursor stage is employed, in which the LES with sufficient simulation duration is used to generate the ABL wind fields. The size of calculation domain in three directions are 3000 m, 1000 m and 1000 m, respectively, as shown in Fig. 3. The mesh resolution in the three directions is 10 m, and the corresponding number of cells is 3 million. The cyclic boundary conditions are employed for four lateral boundaries. The top boundary is set to slip condition, where geostrophic wind direction is regarded as horizontal at this height. Note that this study is a wall-modeled LES, we employ the Moeng surface stress model (Moeng, 1984) to calculate the shear stress at the surface, and surface roughness of 0.001 is chosen as the representative sea surface condition. At the initial time instant, uniform wind with speed of 11.4 m/s fills the whole computational domain (including four vertical boundaries), and the wind direction is 270° corresponding to west wind inflow. The simulation time of precursor stage is 18000s, with the purpose of developing quasi-equilibrium ABL wind field, and the time step is 0.2s. Besides, in order to generate the time histories of inflow boundary for simulation of successor stage, an additional continuity simulation of 1000s is performed.

3.3. Successor stage

The aim of successor stage is to simulate the FOWT under combined ABL wind field generated in the precursor stage and incident waves. Note again that the wake modeling of FOWT is based on the combination of the LES and the ALM considering platform motions, while the dynamic responses are simulated by FAST code. The computational domain and resolution of background mesh are identical to that of the precursor stage, more specifically, 3000m × 1000m × 1000m and 10m × 10m × 10m in x-, y- and z-axis directions, respectively. The wind turbine is located downstream 800 m of the inflow boundary, as shown by the black solid line in Fig. 4. A two-level mesh refinement with hexahedral area is conducted, with the aim of capturing flow details of wind turbine wakes accurately. The size of first-level mesh refinement domain in x-, y- and z-axis directions are 13D, 4D and 3D, respectively, where D denotes the rotor diameter of 126 m. For the hexahedral domain of first-level

Table 1
The gross parameters of the NREL 5 MW wind turbine.

Term	Value
Rated power	5 MW
Rotor orientation	Upwind
Blade number	3
Rotor, hub diameter	126 m, 3 m
Hub height	90 m
Cut-in, rated, cut-out wind speed	3 m/s, 11.4 m/s, 25 m/s
Cut-in, rated rotor speed	6.9 rpm, 12.1 rpm

Table 2
The gross properties of OC4 semi-submersible floating platform.

Term	Value
Draft	20 m
Elevation of platform top	10 m
Elevation of offset columns	12 m
Platform mass	13,473,000 kg
Displacement	13,986.8 m3
Centre of mass	(0 m, 0 m, 13.5 m)

Table 3

The gross parameters of the mooring system.

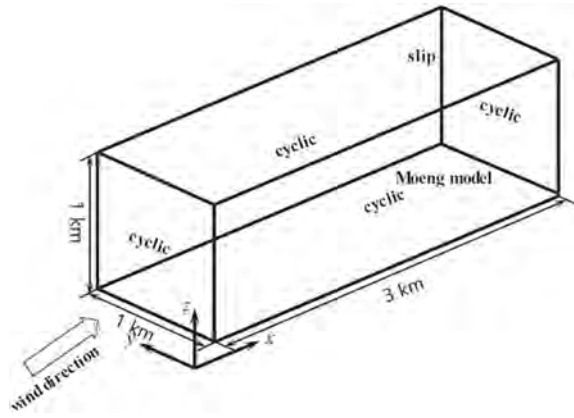| Term	Value
Depth to anchor, fairlead	200 m, 14 m
Radius to anchor, fairlead	853.7 m, 40.868 m
Length, diameter of mooring line	835.5 m, 0.0766 m
Equivalent line mass density, extensional stiffness	113.35 kg/m, 753.6 MN

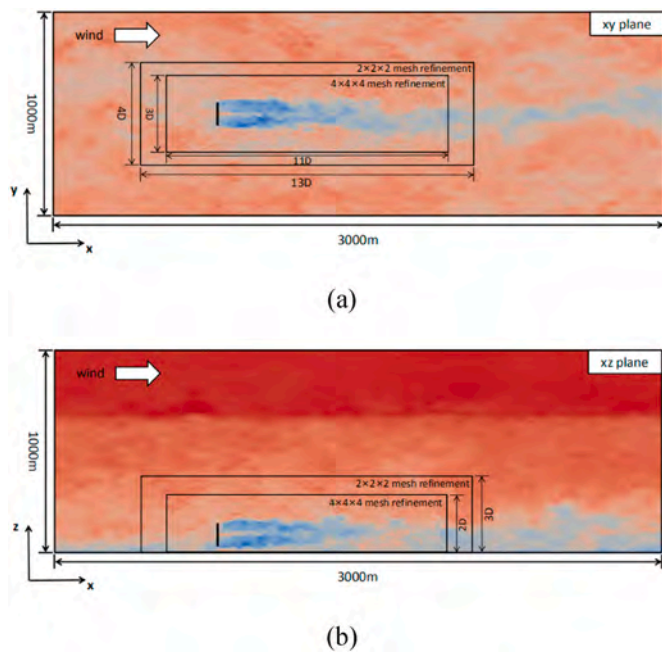**Fig. 3.** The computational domain and boundary conditions of the precursor stage.

Fig. 4. The computational domain and mesh refinement of the successor stage: (a) xy plane and (b) xz plane.

mesh refinement, the wind turbine is positioned 3D from the upstream boundary. With respect to the second-level mesh refinement, the hexahedral domain is reduced by 2D, 1D and 1D in three directions, respectively. Mesh resolution around the wind turbine is 2.5m × 2.5m × 2.5 m, and the mesh number is 12 million.

The boundary conditions of successor stage are also identical to those of precursor stage, except the upstream and downstream boundaries. Specifically, the upstream boundary is modified to mapping condition of time histories, with the purpose of using atmospheric wind data saved in the precursor stage. The downstream boundary is modified to zero

gradient condition to prevent the turbine wakes to cyclically enter upstream boundary. The simulation time of successor stage is 1000s, which is consistent with the additional simulation time of precursor stage for generation of time histories of boundary conditions. When the FOWT is introduced to ABL wind field, the time step is reduced to 0.02s to satisfy the CFL convergence condition. We exclude the first 300s data for the analysis of results to eliminate transient effects of wind turbine startup.

We employ the aero-hydro-servo simulation code FAST for the simulations of OC4 semi-submersible FOWT. Note again that the velocities of wind turbine are resolved and sampled by the LES framework, therefore, the momentum part of blade element momentum theory in AeroDyn is replaced by the ALM and InflowWind module is inactive. The simulation time in FAST is 1000s, whereas the time step is 0.005s, indicating four steps of FAST simulation are available in a time step of LES framework.

3.4. Inflow conditions

The inflow conditions of combined wind and wave simulations are illustrated in Table 4. The atmospheric turbulence inflow with wind speed of 11.4 m/s at hub height is employed as the inflow wind condition, which is generated using the LES with sufficient simulation duration in precursor stage. The wave condition is Stokes first-order regular wave with wave height and wave period being 7.58 m and 12.1s, respectively. It is noted that the LES incorporated with ALM is used to resolve the flow field. After that, the LES framework samples the wind velocities on turbine blades and delivers them to the FAST for fully-coupled dynamic responses. Subsequently, the positions and body forces of wind turbine are updated and fed back to the LES framework for simulation of next time step. We also conduct a baseline case with fixed platform degrees to study the effects of platform motions on aerodynamics and wakes of the FOWT.

4. Numerical validations

4.1. Dynamic responses of wind turbine

In order to validate the reliability and accuracy of the numerical framework used in present work, the aerodynamic performance of BFWT and hydrodynamic responses of FOWT are compared with other numerical methods. Fig. 5 illustrates the rotor power and rotor thrust of BFWT with different steady wind speeds, it is concluded that the aerodynamic performance of BFWT is accurately predicted in this work, compared to the results of Cheng et al. (2019) and FAST engineering code. Fig. 6 shows the surge motion and pitch motion of FOWT with different numerical methods. Note that the steady wind speed is 11 m/s as consistent with Tran et al. (Tran and Kim, 2016a), while the incident wave is the same as in Table 4. The surge motion and pitch motion of FOWT simulated by present work show a good agreement with those of Tran et al. (Tran and Kim, 2016a) and FAST engineering code, although some small differences are observed. Consequently, the numerical framework used in this work has the ability to accurately predict the aerodynamics and wakes of FOWT.

4.2. Simulated ABL wind field

To ensure the dynamic responses of FOWT subjected to ABL wind

Table 4

The inflow conditions of the cases.

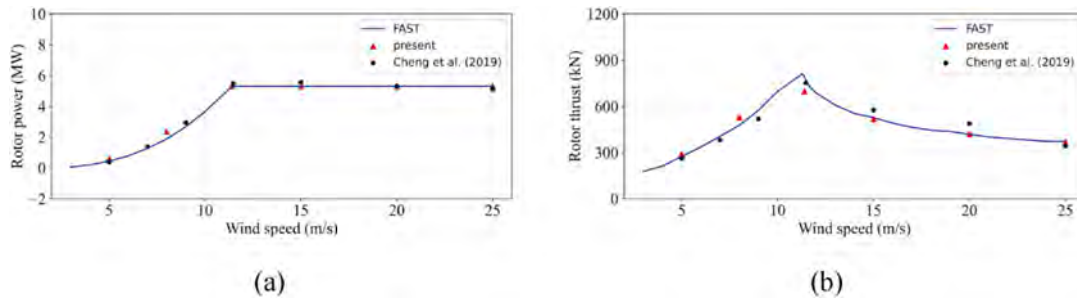| Case	Wind	Wave	Platform motions
Fixed	Atmospheric inflow:11.4 m/s at hub height	Stokes first-order regular wave: H = 7.58 m, T = 12.1s	Fixed
Floating			Released

Fig. 5. Aerodynamic performance of BFWT with different numerical methods: (a) rotor power; (b) rotor thrust.
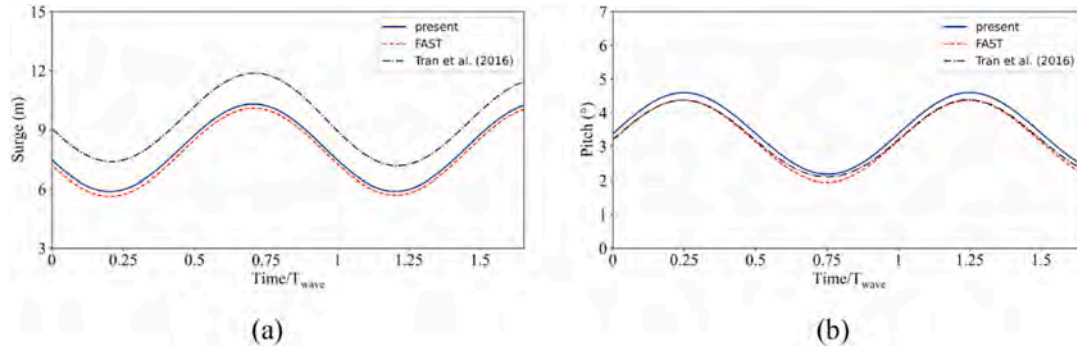

Fig. 6. Platform motions of FOWT with different numerical methods: (a) surge; (b) pitch.

field are correctly evaluated, it is important to validate the characteristics of ABL wind field generated by the LES. Fig. 7 shows the time-averaged vertical profiles of wind velocity, wind direction and turbulence intensity with three components. The wind shear is reproduced due to the roughness of sea surface, and the time-averaged wind speed at hub height is well matched with the rated wind velocity of 11.4 m/s. What's more, the simulated profile of wind speed shows the desired logarithmic law. Due to the fact that Coriolis force caused by earth rotation is take into consideration, the wind direction deflects to right with height, which is not reproduced by the stochastic turbulence model (Doubrawa et al., 2019). Three components of turbulence intensity are presented, in which the turbulence intensity at hub height in x-, y- and z-axis directions are 4.68%, 3.27% and 1.45%, respectively.

Fig. 8 presents the time histories of three components of wind velocity sampled at a point located at hub level. It is shown that the velocities of three components vary drastically throughout the time domain, and the amplitude of oscillations is over 2 m/s. In addition, the power spectrums of velocity fluctuations in the hub height plane are

exhibited. The power spectrums show a good agreement with the $-5/3$ slope (Pope, 2000), indicating that the energy cascade from large scales to small scales are well reproduced by the LES (Churchfield et al., 2012a).

5. Numerical results

5.1. Floating platform motions

The discrepancies of aerodynamic responses and wake characteristics between the FOWT and the BFWT are attributed to the motion of floating platform. Therefore, Fig. 9 shows the platform motions of the FOWT. As it is shown, the time-averaged sway and roll are -0.005 m and $0.23°$, with small amplitude variations. In addition, the mean value and amplitude of yaw are $-0.02°$ and $1.3°$, respectively. It is believed that the influences of the above three platform motions on aerodynamic responses and wake characteristics are negligible. The platform surge exhibits changes with smaller but irregular amplitude, whereas this
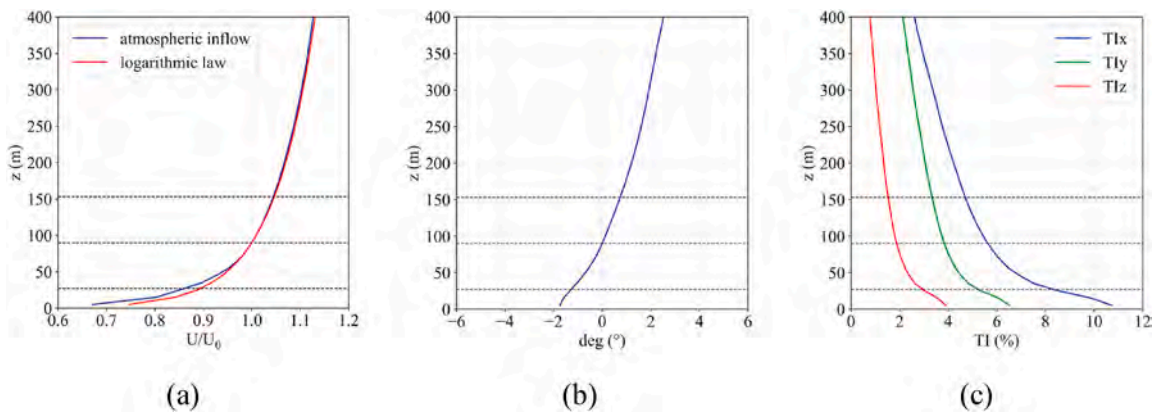

Fig. 7. The time-averaged vertical profiles of the generated quasi-equilibrium ABL wind field: (a) wind velocity; (b) wind direction; (c) turbulence intensity. Three dashed lines denote the top, middle and bottom of rotor area, respectively.
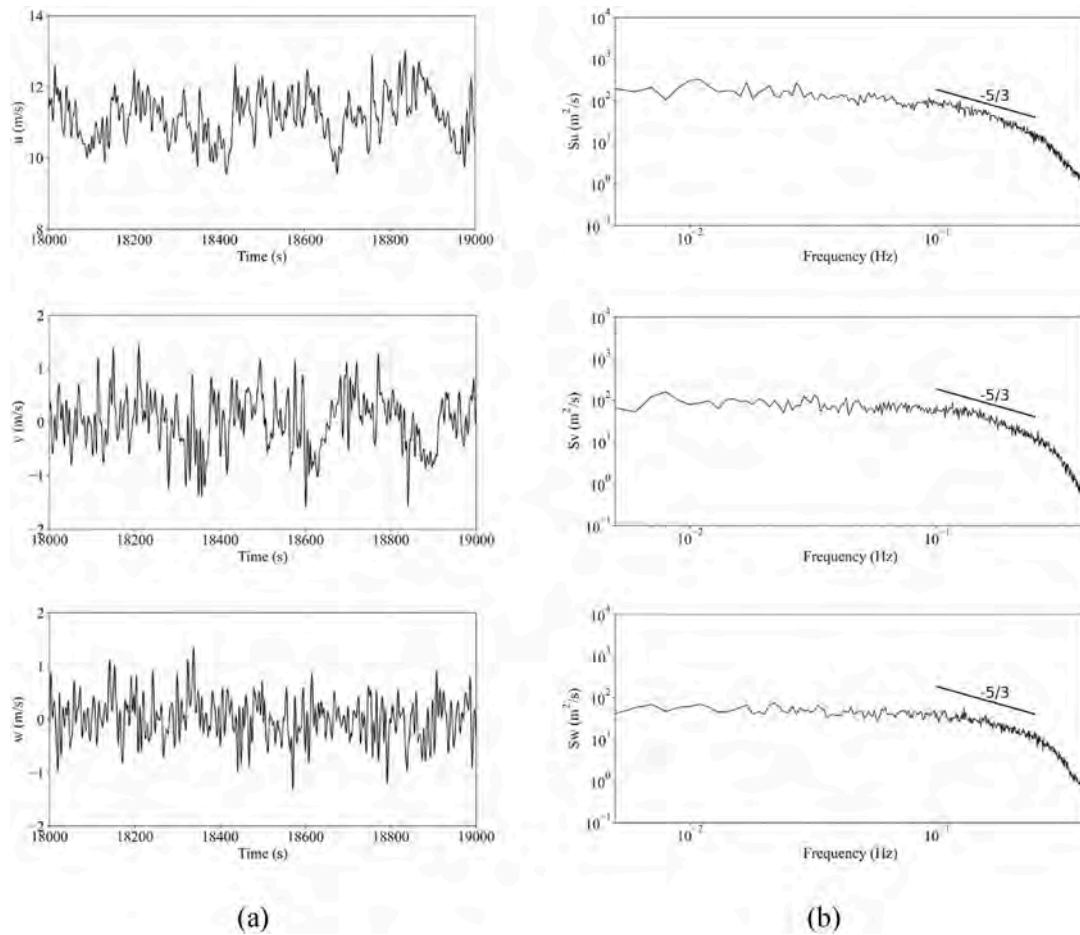
Fig. 8. The three components of the wind velocity: (a) time histories sampled at a point located at the hub height; (b) power spectrums of the velocity fluctuations in the hub height plane.

irregular variation is not evident for the heave. However, if a lighter floating platform is employed, i.e., the spar buoy platform, the platform heave may exhibit irregular variation due to the contribution of vertical component of aerodynamic thrust. The mean value of the pitch motion is 3.1°, in addition, the periodic variation caused by regular wave and the irregular variation due to aerodynamic thrust are observed.

5.2. Power generation

The aerodynamic power outputs of the FOWT and BFWT are illustrated in Fig. 10. The variation of aerodynamic power is caused due to the turbulence structures inside ABL wind field. In addition, the low power output lasting more than 50s is clearly observed. The variation of aerodynamic power of FOWT is exacerbated due to the platform motions excited by incident wave, compared to that of the BFWT. In order to provide a quantitative insight, Table 5 shows the statistics of aerodynamic power of the two wind turbines, including the values of maximum, minimum, mean, root mean square and standard deviation. The mean aerodynamic power of FOWT is 5.17 MW, which is almost identical to the BFWT of 5.20 MW. Because of the effects of platform motions, the maximum and standard deviation of aerodynamic power of the FOWT are higher compared to that of the BFWT, while the minimum is decreased. However, the variation of aerodynamic power induced by platform motions (reflected by discrepancy of the power output between the two scenarios) is not sufficient compared to that of the atmospheric turbulence (reflected by the power output of BFWT). Consequently, it can be concluded that compared to platform motions, the variation of power output of the FOWT under the specified wind-wave in this paper

is more dominated by atmospheric turbulence.

Two time instants from Fig. 10 are selected to further explore the potential reasons for the variation of aerodynamic power. The first moment is 18330s for analysis of relative higher aerodynamic power, and the second moment is 19000s for relative lower aerodynamic power scenario. It is noted that the selected moments for wind turbine simulations are 330s and 700s, due to the fact that first 18000s is used to generate the quasi-equilibrium ABL wind field. Fig. 11 illustrates the contours of instantaneous streamwise velocity in hub height plane for the two selected moments. Only the velocity contours of the FOWT are presented, whereas those of the BFWT are not exhibited due to the similar characteristics. The large-scale turbulence structures with high velocity, the wind turbine wakes with low velocity, the wake meandering and the wake recovery are clearly visualized. In addition, it is found the inflow wind velocity on rotor plane at 18330s is higher than that at 18700s, which is responsible for the higher aerodynamic power.

5.3. Structure responses

In this section, the yaw moment of wind turbine rotor, the blade-root out-of-plane shear force and bending moment of one blade are examined. The yaw moment denotes bending moment about the yaw axis of nacelle. The blade-root out-of-plane shear force denotes shear force at blade root caused by aerodynamic force exerted on wind turbine blade, and the out-of-plane bending moment is caused by shear force distributed along the blade. More detailed definitions about these three quantities can be obtained in (Jonkman and Buhl, 2005). The yaw moment is analyzed to have a possible insight and reference for the yaw
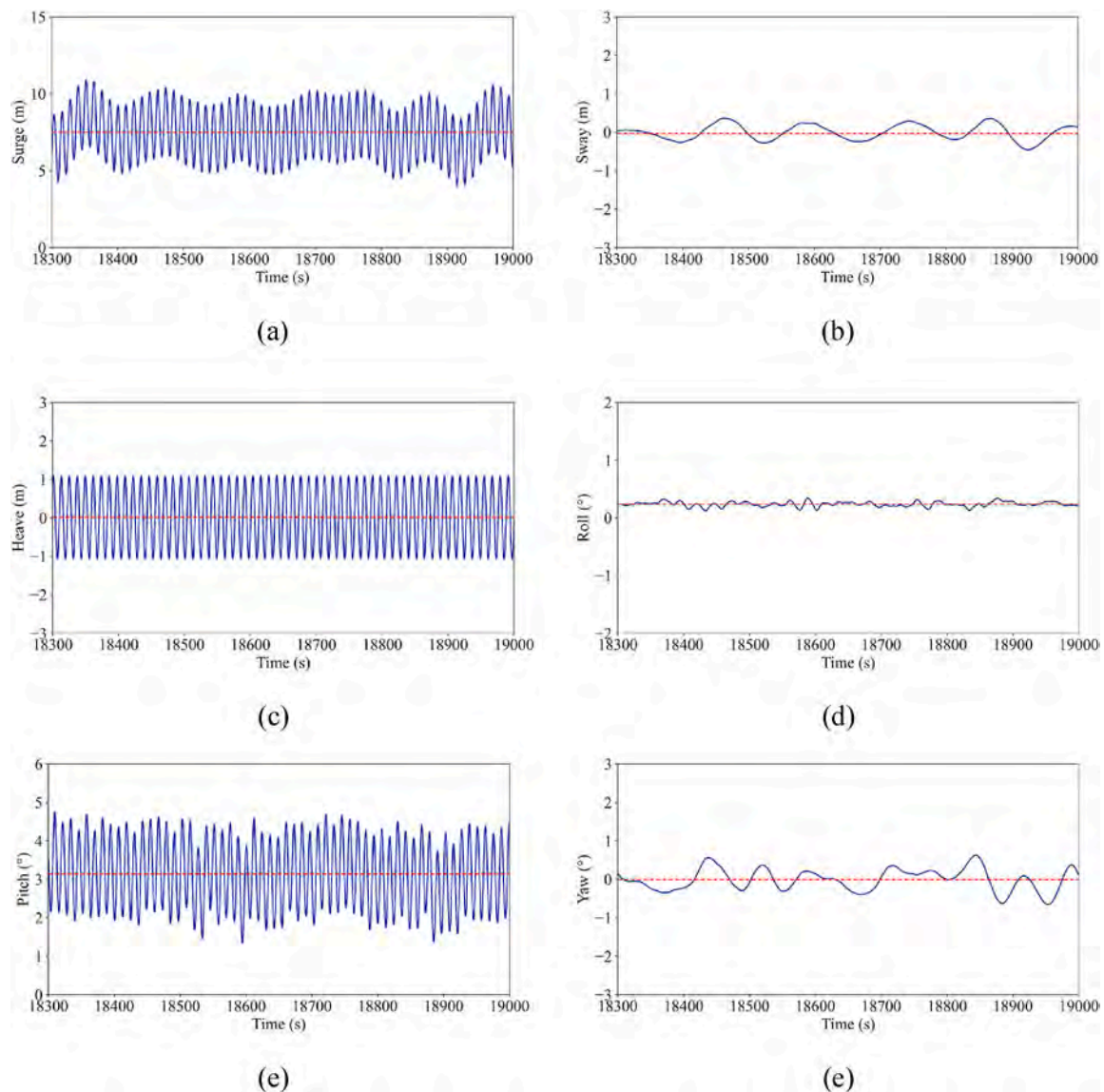
(a) (b) (c) (d) (e) (e)

Fig. 9. The platform motions for the FOWT. The red dotted line represents the time-averaged value.
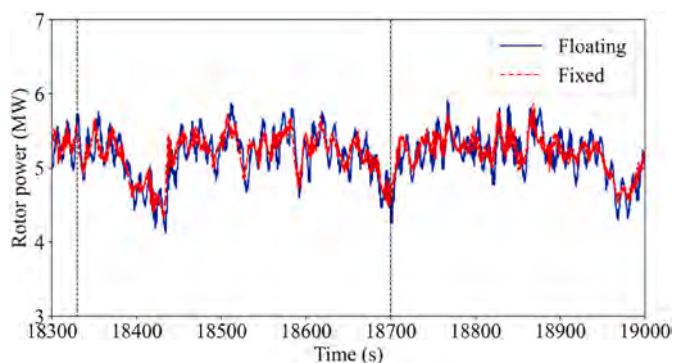

Fig. 10. The aerodynamic power of the FOWT and the BFWT. Two black dotted lines denote the moments of relative higher and lower aerodynamic power, corresponding to the simulation time of 18330s and 19000s (330s and 1000s of wind turbine simulations).

Table 5
The statistics of aerodynamic power for the two wind turbines.

Case	Aerodynamic power (MW)				
	Max	Min	Mean	Rms	Std
Floating	5.91	4.13	5.17	5.18	0.31
Fixed	5.86	4.32	5.20	5.20	0.26

and blade, in which the structure fatigue and failure are significantly suffered.

Fig. 12 illustrates the yaw moment of the FOWT and the BFWT. The complex variation on yaw moment is observed, which can also be attributed to the complex atmospheric inflows. More specifically, the variation of yaw moment in time domain is dramatic, and its value at 18830s is significant. Compared to the BFWT, the yaw moment of the FOWT presents a slightly enhanced amplitude. However, the enhanced amplitude is insignificant compared with the hugely variations induced by atmospheric turbulence. Table 6 illustrates the statistics of yaw moment for the floating and bottom-fixed scenarios. The amplitudes of the floating and bottom-fixed scenarios are 3617 kN m and 3304 kN m, respectively. The increased amplitude due to platform motions is 331
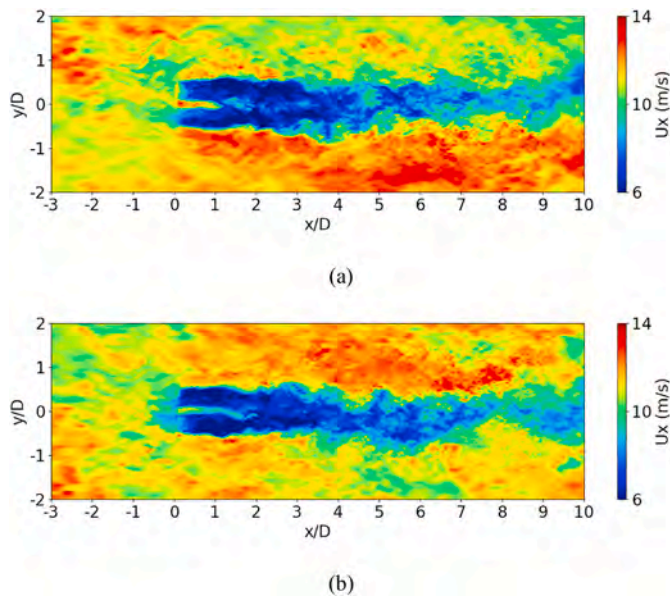
control of the FOWT subjected to ABL wind field. Besides, the blade-root out-of-plane shear force and bending moment are investigated due to the fact that the blade root is a key position of the connection between hub

Fig. 11. The contours of instantaneous streamwise velocity in hub height plane for the FOWT: (a) 18330s and (b) 18700s.
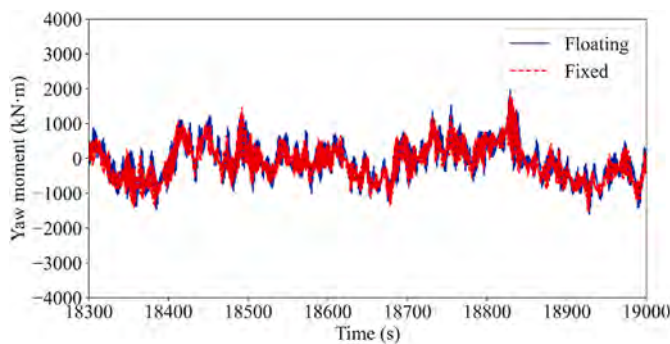

Fig. 12. The yaw moment of the FOWT and the BFWT.

Table 6
The statistics of yaw moment for the two wind turbines.

Case	Yaw moment (kN·m)				
	Max	Min	Mean	Rms	Std
Floating	2021	−1596	−78	539	534
Fixed	1802	−1502	−123	530	516

kN m, which is insignificant compared to the amplitude of yaw moment of BFWT. In addition to amplitude, the distinctions of root mean square and standard deviation between the two scenarios are also not evident. Therefore, in the implementation of active yaw control on floating wind farms to maximize power generation, more efforts should be dedicated on the significant yaw moment caused by atmospheric turbulence rather than the slightly increased values due to platform motions.

Fig. 13 shows the power spectrum of yaw moment for the FOWT and the BFWT. The peak of blade-passage frequency f_b is the most visible, which is three times of rotor revolution frequency. The multi-scale turbulent structures exist in the atmosphere, where the turbulence scales vary from the order of mm to km (Stull, 1988). Consequently, the force exerted on wind turbine blades has a wide frequency range, leading to the visible peaks of harmonics multiple of blade-passage frequency f_b. Besides, it is shown that the amplitudes are decreased with increasing frequency. Compared to the BFWT, the yaw moment
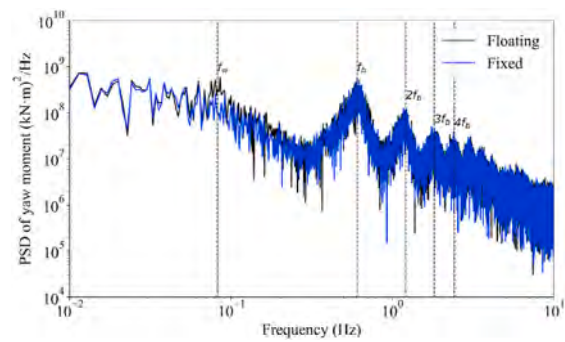

Fig. 13. The power spectrum of yaw moment for the FOWT and the BFWT. The f_w and f_b are incident wave frequency and blade-passage frequency, respectively, and y-axis denotes the power spectrum density.

spectrum of the FOWT exhibits the peak of incident wave frequency f_w. However, the amplitude of this frequency peak is not significant, reflecting the minor effects of platform motions on yaw moment.

The time histories of out-of-plane shear force and bending moment for one blade are illustrated in Fig. 14. The out-of-plane shear force of the BFWT shows a complex characteristic due to the contributions of wind shear and atmospheric turbulence. Because of the increased horizontal component of blade gravity attributed to platform pitch motion, the enhanced tend for floating scenario is visualized. Since the out-of-plane bending moment is caused by shear force, the similar conclusion is concluded. Moving towards the quantitative analysis of out-of-plane shear force and bending moment, as presented in Table 7. The enhanced mean value of out-of-plane shear force caused by platform motions is 10.7 kN, which is insufficient compared to the mean value of the bottom-fixed scenario and consistent with the above analysis of yaw moment. However, a distinction from the yaw moment is that the increased standard deviation of floating scenario is more notable compared to that of bottom-fixed one. The same conclusion can be addressed for the analysis of out-of-plane bending moment.

Fig. 15 shows the corresponding power spectrums of the above two quantities for the FOWT and the BFWT. The peak of rotor revolution frequency f_r is visible, reflecting the asymmetry of vertical load distribution due to the wind shear and turbulence in atmosphere. Consistent with the spectrums of the yaw moment, the peaks of harmonics of rotor revolution frequency f_r are visible and its amplitudes decrease with increasing frequency. Additionally, the peak of incident wave frequency f_w for the FOWT is observed compared to the bottom-fixed case, which indicates that the loads on rotor root are highly related to the platform motions excited by incident waves. The peaks of two additional frequencies on the both sides of rotor revolution frequency f_r, 0.12 Hz and 0.28 Hz are evident. The two frequencies were also found on the normal force at the section of 0.8 times rotor radius of the blade (Wang et al., 2021). Note that the rotor revolution frequency f_r is approximately 0.21 Hz at the rated wind speed, and a decreased rotor revolution frequency is available at below rated wind speed. Therefore, in order to avoid the fatigue loads and failure of the blade root caused by the frequency resonance between the rotor revolution frequency and the two additional frequencies, additional considerations of rotor revolution frequency under operational conditions must be included.

5.4. Wake velocity

Due to the wind energy extracted from the wind field, the turbine wakes show decreased wind speed and increased turbulence intensity. Figs. 16 and 17 show the contours of time-averaged streamwise velocity of horizontal and vertical planes for the FOWT and the BFWT, with the purpose of providing a visual insight of wind turbine wakes. For the velocity contours of horizontal plane, the wake width increases as the wake travels downstream. The velocity deficit in turbine wakes is still
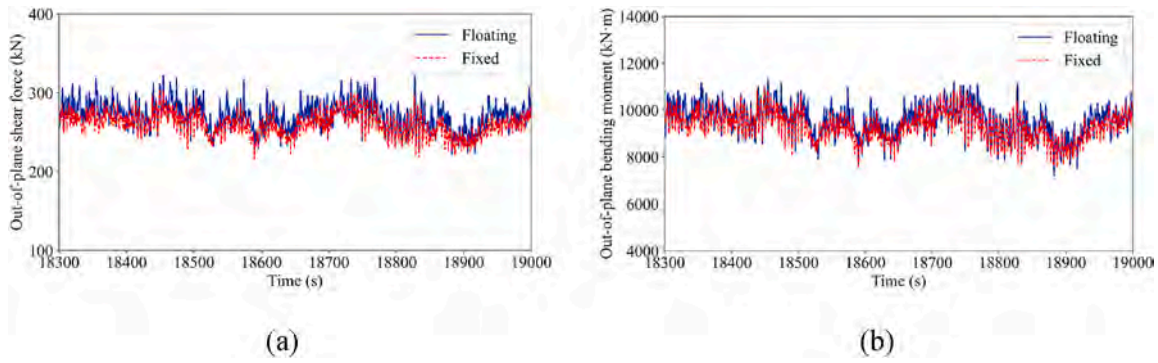
Fig. 14. The structure responses of blade root for floating and bottom-fixed scenarios: (a) out-of-plane shear force; (b) out-of-plane bending moment.

Table 7
The statistics of out-of-plane shear force and bending moment for the two wind turbines, including the values of maximum, minimum, mean and standard deviation.

Case	Out-of-plane shear force (kN)				
	Max	Min	Mean	Rms	Std
Floating	322.3	221.8	270.9	271.5	17.33
Fixed	303.0	215.8	260.2	260.6	14.25
Case	Out-of-plane bending moment (kN·m)				
	Max	Min	Mean	Rms	Std
Floating	11330	7204	9556	9580	668
Fixed	10920	7545	9318	9337	594

evident even at 10D, which means that the downstream wind turbines are inevitably sited in the wakes of upstream wind turbines, particularly when the wind direction is aligned with wind farm layout. There are no noticeable visualizable differences between the floating and bottom-fixed scenarios. For the velocity contours in vertical plane, as shown in Fig. 17, the region influenced by wind turbine wakes and the growth of wake height are visualized. The wake recovery of the floating scenario is a little faster than that of the bottom-fixed scenario, as reflected after 8D. Besides, the wake center of the FOWT is slightly higher, which can be attributed to platform static pitch.

The wind turbine wakes can be divided into near-wake and far-wake based on the downstream distance from the wind turbine, and a typical length of near-wake region is 2–4 rotor diameters (Vermeer et al., 2003). When the wind turbine is modeled by the ALM, the flow details in near-wake region are not well captured compared to that of the blade-resolved modeling. Therefore, Abkar and Porté-Agel (2015) presented the velocity deficit of wind turbine wakes from the downstream

distance 4D to 20D with an interval of 4D, which is typically the far-wake region. Following the above idea, this study presents the horizontal and vertical profiles of wake velocity deficit of the two wind turbines from downstream distance of 4D to a closer far-wake distance of 9D, but with a smaller distance interval of 1D, as shown in Figs. 18 and 19. Due to the interaction between the wind turbine wakes and the ambient atmospheric wind field, the velocity recovery of turbine wakes is observed when the wake travels downstream. For the hub level plane, the asymmetric profile of velocity deficit is visible because of the complexity of atmospheric turbulence inflows.

Small differences of wake deficit between the floating and bottom-fixed scenarios are observed both in horizontal and vertical profiles. For the horizontal profile, the velocity deficit of the FOWT at downstream distance of 4D is more severe than that of the BFWT. However, this conclusion is reversed when the downstream distance is increased to 8D. For the vertical profile of wake deficit, the height of wake center (here approximately the position of maximum velocity deficit) of the FOWT is higher than that of the BFWT, which is consistent with the above analysis of time-averaged velocity contours. Therefore, the wake center is gradually far away from the hub height level when the wakes travel downstream. A more quantitative analysis of the wake center for the two wind turbines is introduced in the following section.

5.5. Wake center

To supply a quantitative insight for the analysis of wake center position, we calculate the time-averaged wake center with the Gauss fitting function, and the results are shown in Fig. 20. It can be seen that the wake center in the horizontal plane deflects to the left when the view is aligned with streamwise direction. Differences of wake center position in the horizontal plane between the FOWT and the BFWT are not evident. However, differences in vertical plane are more visible,
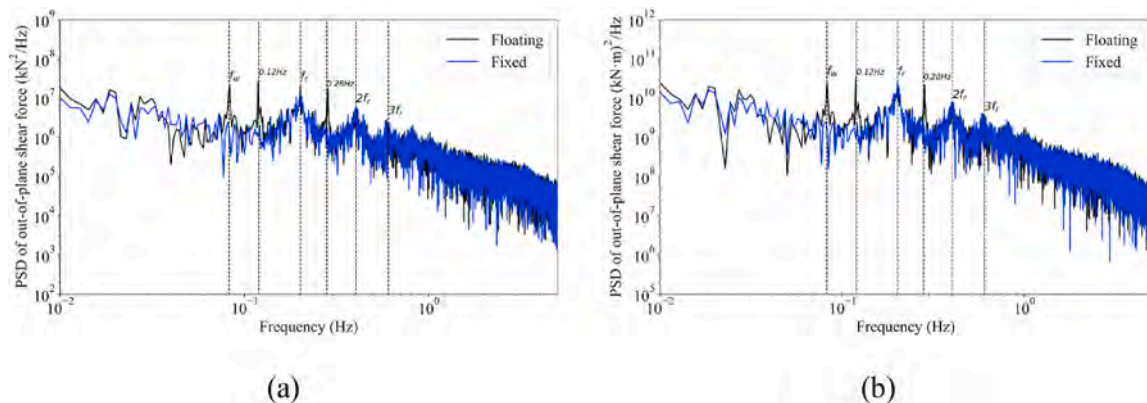

Fig. 15. The power spectrums of blade root structure responses for the FOWT and the BFWT: (a) out-of-plane shear force; (b) out-of-plane bending moment. The f_w and f_r denote incident wave frequency and rotor revolution frequency, respectively.
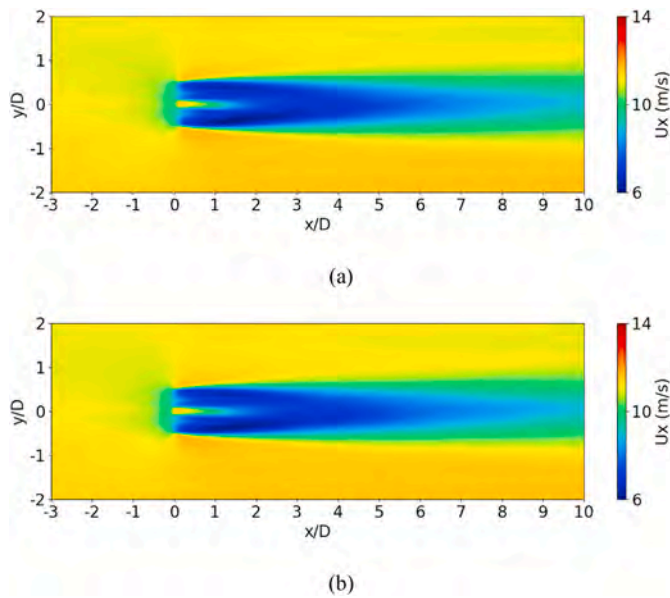
Fig. 16. The contours of time-averaged streamwise velocity of hub height plane for the two wind turbines: (a) the FOWT; (b) the BFWT.
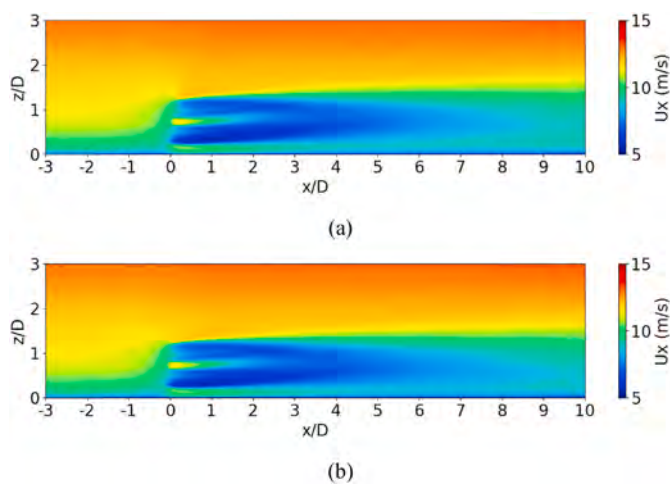

Fig. 17. The contours of time-averaged streamwise velocity of vertical plane through rotor center for the two wind turbines: (a) the FOWT; (b) the BFWT.

particularly for the far wake region such as 10D downstream distance. Specifically, the wake center height of the bottom-fixed scenario is approximately 0.8D, 0.1D higher than the hub height level. The wake center height of the floating scenario is approximately 0.9D, which is beneficial for the aerodynamic performance of downstream wind turbines because the wakes are driven far away from the hub height level due to the platform static pitch. Consequently, if the vertical staggered arrangement by changing tower height of floating wind farm is performed to improve the annual power generation, the wake deflection caused by the platform static pitch needs an additional consideration.

In addition to the time-averaged wake centers, we also present the instantaneous wake center of vertical plane at 5D and 7D downstream distances for the two wind turbines, as illustrated in Fig. 21. Note that the wake center position in the horizontal plane is not shown here because of the minor differences between the two wind turbines. Consistently with the analysis above, the wake center of the floating scenario is slightly higher than that of the bottom-fixed scenario. Besides, we can clearly observe that the wake center position changes over time, which is referred to the effect of wake meandering. The difference

between bottom-fixed and floating is enhanced with increasing downstream distance. Consequently, the downstream wind turbines may be affected by the partial wakes of upstream wind turbines, leading to increased fatigue loads of downstream wind turbines.

In order to understand the upward motion of wake center, two typical time instants are selected, one is 18410s for 5D downstream distance from wind turbine and another is 18440s for 7D downstream distance. Fig. 22 shows the instantaneous contours of streamwise velocity for the two specified moments. Note that the contours for the bottom-fixed scenario are not presented because it is not possible to distinguish any difference with respect to the FOWT case by simple visual inspection. At 18410s, the wake expansion is evidently visible at 5D due to the breakdown of the wakes approximately at 3D. The outside atmospheric flow can easily enter the wind turbine wakes as shown at 18440s at 7D downstream distance. Consequently, the large deflection of wake center highly depends on the mixing of the turbine wakes with the external atmospheric turbulence.

5.6. Turbulence intensity

Another important factor for wind turbine wakes is turbulence intensity, which is highly responsible for fatigue loads of downwind turbines (Rosen and Sheinman, 1996). We define the turbulence intensity $TI = \sqrt{1/3(I_x^2 + I_y^2 + I_x^2)}$, where I_x, I_y and I_z are the three components of turbulence intensity. Some previous efforts have demonstrated that the time-averaged turbulence intensity (averaged in the last 700s) for the FOWT wakes is almost identical to that of the BFWT. Hence, the time-averaged plots of turbulence intensity are not shown here. The alternatives are instantaneous turbulence intensity of last time instant (19000s) at the horizontal hub plane and the vertical plane through rotor center. As illustrated in Fig. 23, the turbulence intensity is significantly enhanced in the wind turbine wakes. The turbulence intensity at downstream 1D is significant, indicating that the shear layer between turbine wakes and the outer atmosphere is quickly breakdown. In Fig. 24, the turbulence intensity in wind turbine wakes from downstream distance of 1D to 7D is significant, which can induce fatigue loads on downstream wind turbines. After the downstream wake distance of 7D, the turbulent intensity gradually decreases. Some subtle distinctions are visualized if we observe carefully the instantaneous contours of turbulence intensity both in horizontal and vertical planes for the two scenarios, for instance, at the positions around the rotor plane, downstream distances of 3D and 7D. However, those distinctions are insignificant because of the complex features of turbulence intensity in wind turbine wakes. Therefore, the effects of floating platform motions on the turbulence intensity in wakes are limited when the wind turbine is subjected to the atmospheric turbulence.

One distinctive characteristic of atmospheric turbulence is the large-scale turbulence, as shown in Fig. 24, which has significant effects on wind turbine wakes. The instantaneous turbulence intensity between various computational moments (not shown here) have demonstrated distinct differences. Therefore, in order to examine the potential influences of large-scale atmospheric turbulence on wind turbine wakes, we present the instantaneous contours of turbulence intensity of a vertical plane located at downstream distance of 7D, a typical spacing between adjacent wind turbines insides wind farms, as shown in Fig. 25. The selected moments for the instantaneous contours are from 18500s to 18900s with an interval of 50s. As expected, the turbulence intensity in wind turbine wakes is significantly enhanced. At 18500s, the maximum value of turbulence intensity occurs at the upper right of the rotor, whereas changes to upper left are visible at 18600s. The spatiotemporal variation of wind turbine wakes is complicated, and this is caused by the motions of large-scale turbulence, also called the wake meandering. The wakes in rotor sweep region of downstream wind turbine are also complex. Therefore, the systematic studies of FOWT wakes and its effects on downstream wind turbines particularly for the fatigue loads and
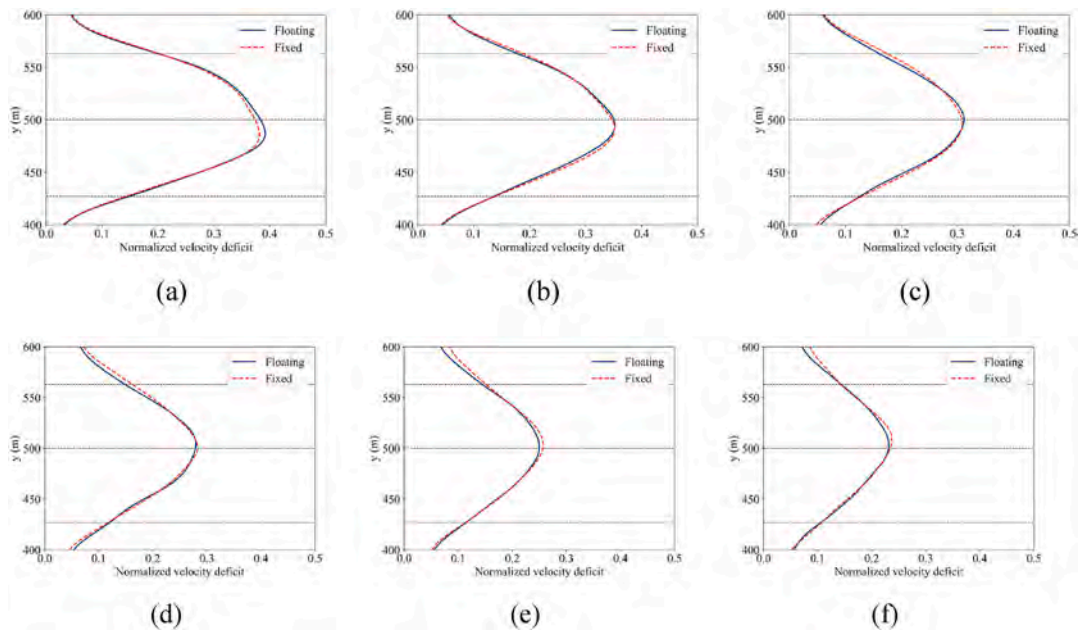
Fig. 18. The normalized wake velocity deficit $\Delta U/U_{hub}$ of hub height horizontal plane for the floating and bottom-fixed scenarios: (a) $x = 4D$; (b) $x = 5D$; (c) $x = 6D$; (d) $x = 7D$; (e) $x = 8D$; (f) $x = 9D$. Three black dotted lines denote left-tip, rotor center and right-tip, respectively.
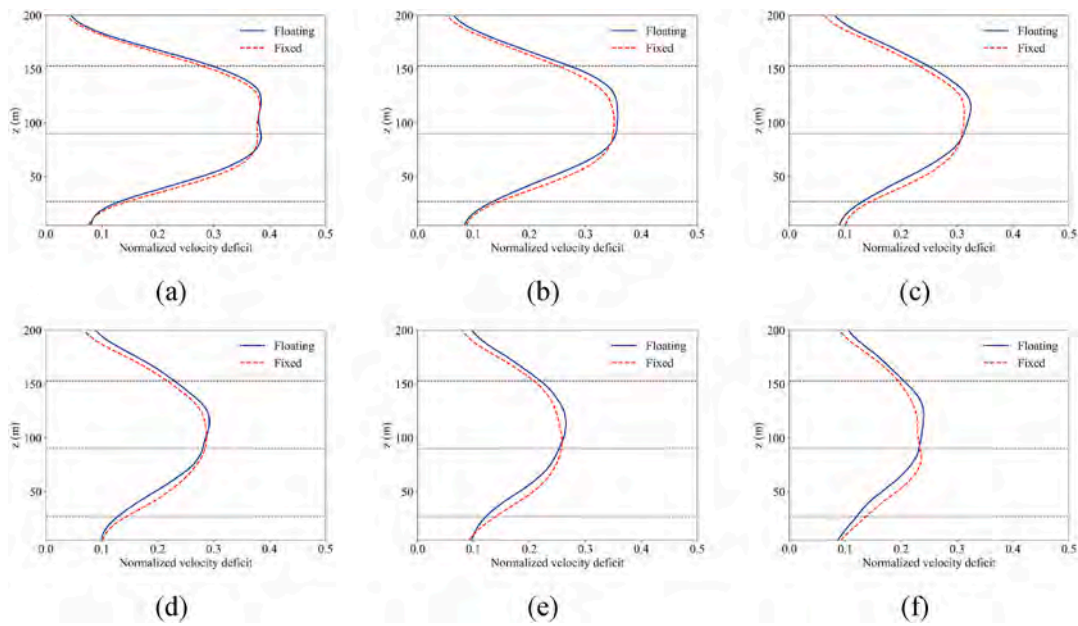

Fig. 19. The normalized wake velocity deficit $\Delta U/U_{hub}$ of vertical plane through rotor center for the floating and bottom-fixed scenarios: (a) $x = 4D$; (b) $x = 5D$; (c) $x = 6D$; (d) $x = 7D$; (e) $x = 8D$; (f) $x = 9D$. Three black dotted lines denote up-tip, rotor center and down-tip, respectively.

the structure failure are recommended.

6. Conclusions

In this study, we conduct the numerical investigation of a FOWT immersed in ABL wind field to investigate the effects of platform motions on aerodynamic responses and wake characteristics. The NREL 5 MW baseline wind turbine mounted on OC4 phase II semi-submersible floating platform is adopted as the simulation model. The quasi-equilibrium ABL wind field is generated by the LES with sufficient simulation duration in precursor stage. The wind turbine wakes and fully-coupled dynamics are simulated in successor stage, in which the ALM is employed to simulate wind turbine aerodynamics and the

potential theory is adopted to solve hydrodynamic forces. Besides, a baseline case of bottom-fixed scenario is also performed for comparison.

The properties of generated ABL wind field are firstly examined, in which the desired wind profile and the $-5/3$ slope for spectrums of velocity fluctuations are reproduced. Then the numerical results of aerodynamic responses are analyzed, including power generation and structure responses. The power variation of FOWT is found to be dominated by ABL wind field, more than platform motions. For the structure responses, the effects of platform motions on yaw moment are negligible. The out-of-plane shear force and bending moment of FOWT are slightly enhanced due to platform motions, besides, the peaks of incident wave frequency and two additional frequencies of 0.12 Hz and 0.28 Hz are clearly visible on the power spectrums. Therefore,
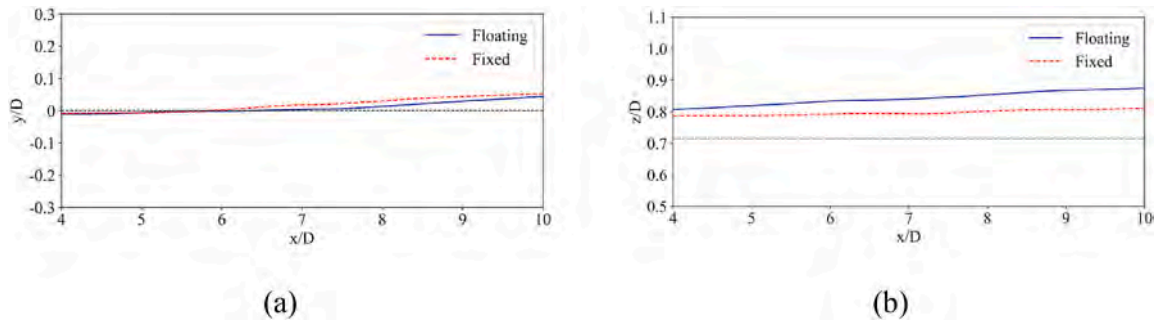
Fig. 20. The time-averaged wake center for the floating and bottom-fixed scenarios: (a) horizontal plane of hub height; (b) vertical plane through rotor center. The Gauss fitting function is used to determine the wake center, and the black dotted lines denote the rotor center.
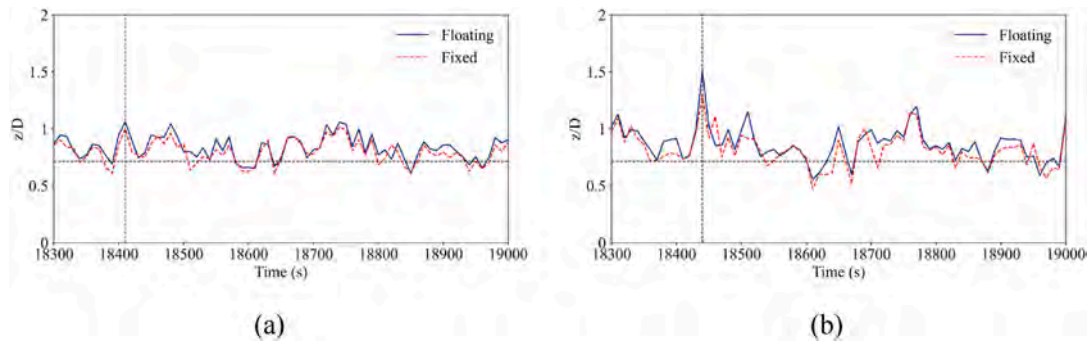

Fig. 21. The instantaneous wake center of vertical plane at different downstream distances for the two wind turbines: (a) downstream distance of 5D; (b) downstream distance of 7D. The horizontal and vertical black dotted lines denote the rotor center and the selected analysis moments (18410s and 18440s for the two subplots), respectively.
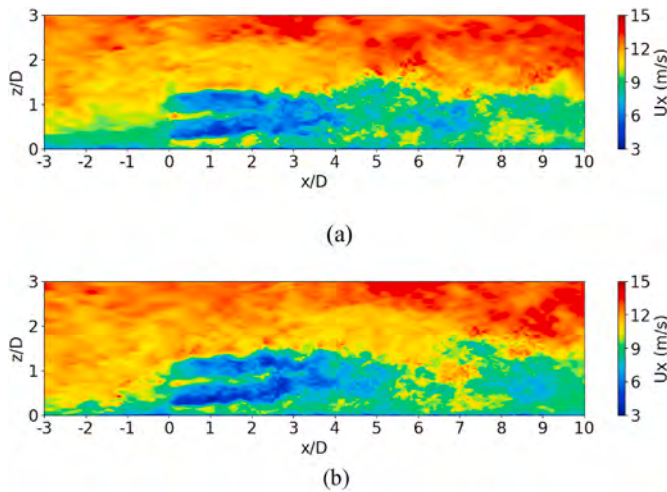

Fig. 22. The instantaneous contours of streamwise velocity of the FOWT for the two specified moments: (a) 18410s for downstream distance of 5D; (b) 18440s for downstream distance of 7D.

Fig. 23. The instantaneous contours of turbulence intensity of hub height plane for the two wind turbines: (a) the floating scenario; (b) the bottom-fixed scenario.

additional considerations of rotor revolution frequency under operational conditions are required for the design of FOWT to avoid structure failure on the blade root, because the frequency resonance occurs if the rotor revolution frequency determined by wind speed is close to 0.12 Hz.

The differences of wake deficit between the floating and the bottom-fixed scenarios are small. However ,the time-averaged wake center of floating scenario is far away from the hub height level because of pitch motion of platform, which is a potential benefit for downstream wind turbines. The variation of wake center is complex around the hub height with time, and significant deflection of wake center is observed due to
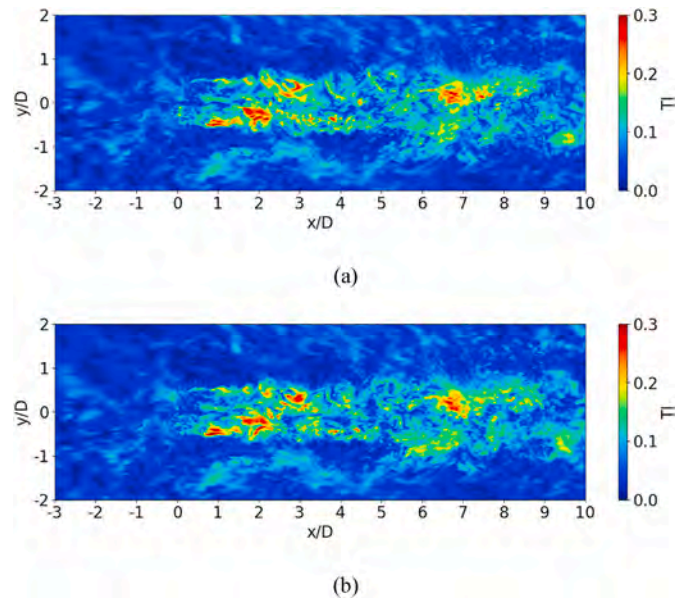
the entrance of external atmospheric flow into wind turbine wakes. The spatiotemporal distributions of turbulence intensity in turbine wakes are so complicated that it is a challenge for the operation of downstream wind turbines. In addition, visually significant differences between the two scenarios are not observed.

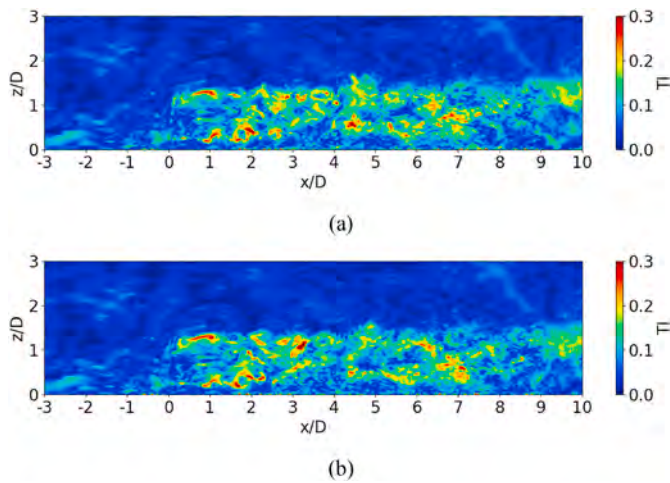Due to the hydrodynamic responses of OC4 semi-submersible FOWT

Fig. 24. The instantaneous contours of turbulence intensity of vertical plane through rotor center for the two wind turbines: (a) the floating scenario; (b) the bottom-fixed scenario.

under the specified incident wave conditions in this paper are small, deviations of aerodynamic responses and wake characteristics between the floating and the bottom-fixed scenarios are insignificant. In further studies, different wind-wave conditions especially extreme marine conditions and different types of floating platforms (i.e., OC3 spar buoy platform) will be conducted to systematically investigate the aerodynamic responses and wake characteristics of the FOWT under ABL inflow. Besides, atmospheric stratification has a significant effect on wind turbine dynamics and wakes. Therefore, the investigations for the FOWT subjected to the stable and convective atmospheric stratifications are also recommended.

Funding

CRediT authorship contribution statement

Shun Xu: Data curation, Writing – original draft, preparation, Visualization, Investigation, Software, Validation. **Tiegang Zhuang:** Investigation, Validation. **Weiwen Zhao:** Data curation, Software,
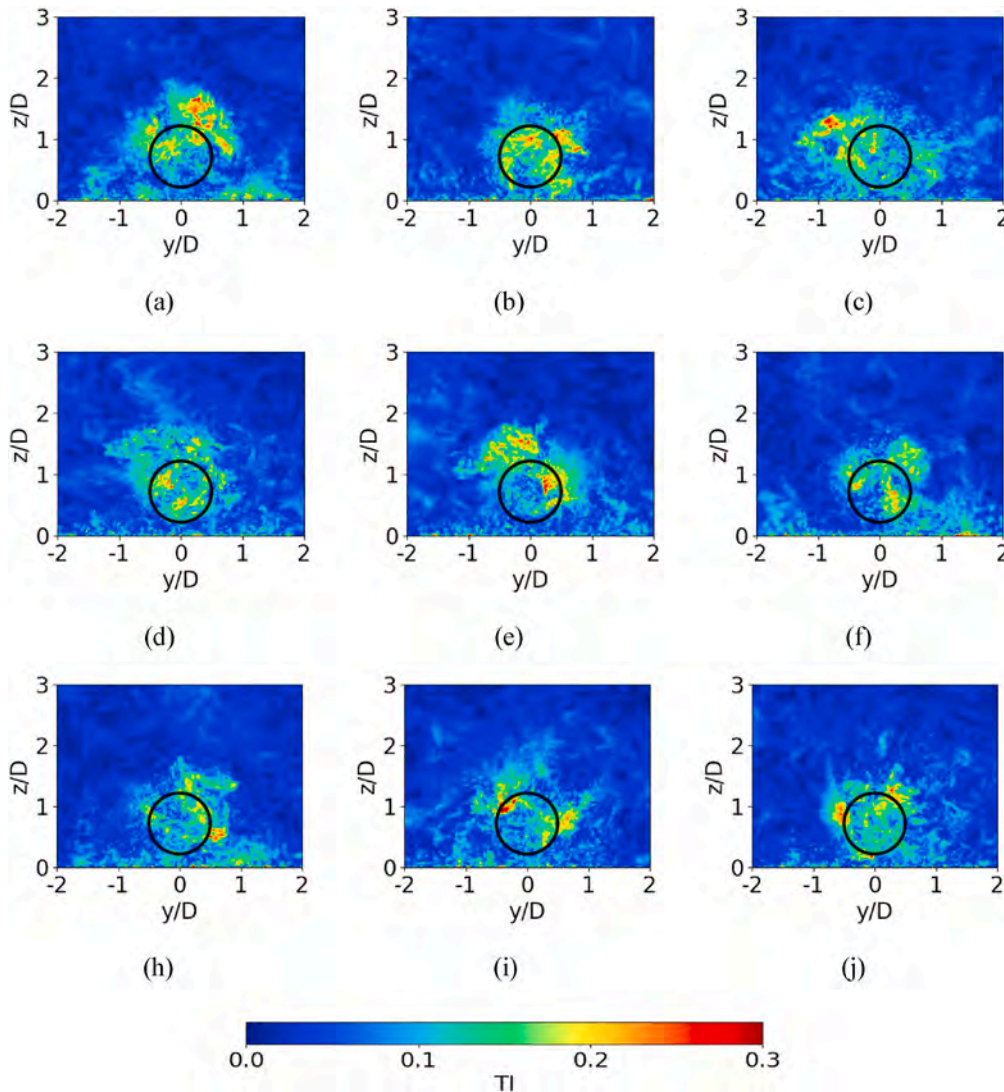
Fig. 25. The instantaneous contours of turbulence intensity of vertical plane located at downstream distance of 7D: (a) 18500s; (b) 18550s; (c) 18600s; (d) 18650s; (e) 18700s; (f) 18750s; (h) 18800s; (i) 18850s; (j) 18900s. The black circle represents the rotor sweep area.

Visualization, Investigation. **Decheng Wan:** Supervision, Conceptualization, Methodology, Investigation, Writing – review & editing.

Declaration of competing interest

Data availability

Data will be made available on request.

Acknowledgements

References

Abkar, M., Porté-Agel, F., 2015. Influence of atmospheric stability on wind-turbine wakes: a large-eddy simulation study. Phys. Fluid. 27 (3), 035104.

Amaral, G.A., Mello, P.C., do Carmo, L.H.S., et al., 2021. Seakeeping tests of a FOWT in wind and waves: an analysis of dynamic coupling effects and their impact on the predictions of pitch motion response. J. Mar. Sci. Eng. 9 (2), 179.

Atcheson, M., Garrad, A., Cradden, L., et al., 2016. Floating Offshore Wind Energy. Springer.

Cheng, P., Huang, Y., Wan, D., 2019. A numerical model for fully coupled aero-hydrodynamic analysis of floating offshore wind turbine. Ocean. Eng. 173, 183–196.

Churchfield, M.J., Lee, S., Michalakes, J., et al., 2012a. A numerical study of the effects of atmospheric and wake turbulence on wind turbine dynamics. J. Turbul. (13), N14.

Churchfield, M., Lee, S., Moriarty, P., 2012b. Overview of the Simulator for Wind Farm Application (SOWFA). National Renewable Energy Laboratory.

Coulling, A.J., Goupee, A.J., Robertson, A.N., et al., 2013. Validation of a FAST semi-submersible floating wind turbine numerical model with DeepCwind test data. J. Renew. Sustain. Energy 5 (2), 023116.

Doubrawa, P., Churchfield, M.J., Godvik, M., et al., 2019. Load response of a floating wind turbine to turbulent atmospheric flow. Appl. Energy 242, 1588–1599.

Eliassen, L., Obhrai, C., 2016. Coherence of turbulent wind under neutral wind conditions at FINO1. Energy Proc. 94, 388–398.

Godvik, M., 2016. Influence of the Wind Coherence on the Response of a Floating Wind Turbine Science Meets Industry, 6th April. Stavanger.

Greenshields, C.J., 2015. OpenFOAM user guide. OpenFOAM Foundation Ltd, version 3 (1), 47.

Gueydon, S., Judge, F.M., O'shea, M., et al., 2021. Round robin laboratory testing of a scaled 10 mw floating horizontal axis wind turbine. J. Mar. Sci. Eng. 9 (9), 988.

Huang, Y., Wan, D., 2019a. Unsteady aerodynamics of a spar-type floating offshore wind turbine induced by platform pitch motion, 09-13 July. In: Proceedings of the 10th International Conference on Computational Methods (Singapore).

Huang, Y., Wan, D., 2019b. Investigation of interference effects between wind turbine and spar-type floating platform under combined wind-wave excitation. Sustainability 12 (1), 246.

Huang, Y., Cheng, P., Wan, D., 2019. Numerical analysis of a floating offshore wind turbine by coupled aero-hydrodynamic simulation. J. Mar. Sci. Appl. 18 (1), 82–92.

Huang, Y., Wan, D., Hu, C., 2021. Numerical analysis of aero-hydrodynamic responses of floating offshore wind turbine considering blade deformation. F. In: Proceedings of the 31st International Ocean and Polar Engineering Conference (OnePetro).

Huang, Y., Xiao, Q., Wan, D., 2022. Wake interaction between two floating offshore wind turbines with blade deformation. F. In: Proceedings of the International Conference on Offshore Mechanics and Arctic Engineering. American Society of Mechanical Engineers.

Johlas, H., Martinez, L., Schmidt, D., et al., 2019. Large Eddy Simulations of Floating Offshore Wind Turbine Wakes with Coupled Platform Motion. National Renewable Energy Lab (NREL), Golden, CO (United States).

Johlas, H., Martínez-Tossas, L., Lackner, M., et al., 2020. Large eddy simulations of offshore wind turbine wakes for two floating platform types. In: Proceedings of the Journal of Physics: Conference Series, F. IOP Publishing.

Jonkman, J.M., Buhl, M.L., 2005. FAST User's Guide. National Renewable Energy Laboratory Golden, CO, USA.

Jonkman, J., Butterfield, S., Musial, W., et al., 2009. Definition of a 5-MW Reference Wind Turbine for Offshore System Development. National Renewable Energy Lab (NREL), Golden, CO (United States).

Kaimal, J.C., Wyngaard, J., Izumi, Y., et al., 1972. Spectral characteristics of surface-layer turbulence. Q. J. R. Meteorol. Soc. 98 (417), 563–589.

Lee, S., Churchfield, M., Moriarty, P., et al., 2012. Atmospheric and wake turbulence impacts on wind turbine fatigue loadings. F. In: Proceedings of the 50th AIAA Aerospace Sciences Meeting Including the New Horizons Forum and Aerospace Exposition.

Li, P., Cheng, P., Wan, D., et al., 2015. Numerical Simulations of Wake Flows of Floating Offshore Wind Turbines by Unsteady Actuator Line Model; Proceedings of the 9th International Workshop on Ship and Marine Hydrodynamics. F. Glasgow, UK.

Li, L., Gao, Y., Hu, Z., et al., 2018a. Model test research of a semisubmersible floating wind turbine with an improved deficient thrust force correction approach. Renew. Energy 119, 95–105.

Li, L., Liu, Y., Yuan, Z., et al., 2018b. Wind field effect on the power generation and aerodynamic performance of offshore floating wind turbines. Energy 157, 379–390.

Lu, H., Porté-Agel, F., 2011. Large-eddy simulation of a very large wind farm in a stable atmospheric boundary layer. Phys. Fluids 23 (6), 065101.

Madsen, H.A., Bak, C., Døssing, M., et al., 2010. Validation and modification of the blade element momentum theory based on comparisons with actuator disc simulations. Wind Energy 13 (4), 373–389.

Mann, J., 1994. The spatial structure of neutral atmospheric surface-layer turbulence. J. Fluid Mech. 273, 141–168.

Masciola, M., Robertson, A., Jonkman, J., et al., 2013. Assessment of the Importance of Mooring Dynamics on the Global Response of the DeepCwind Floating Semisubmersible Offshore Wind Turbine; Proceedings of the the Twenty-Third International Offshore and Polar Engineering Conference. F, OnePetro.

Matha, D., Schlipf, M., Pereira, R., et al., 2011. Challenges in Simulation of Aerodynamics, Hydrodynamics, and Mooring-Line Dynamics of Floating Offshore Wind Turbines; Proceedings of the Twenty-First International Offshore and Polar Engineering Conference. F (OnePetro).

Meneveau, C., 2019. Big wind power: seven questions for turbulence research. J. Turbul. 20 (1), 2–20.

Moeng, C.-H., 1984. A large-eddy-simulation model for the study of planetary boundary-layer turbulence. J. Atmos. Sci. 41 (13), 2052–2062.

Ning, X., Wan, D., 2019. LES Study of wake meandering in different atmospheric stabilities and its effects on wind turbine aerodynamics. Sustainability 11 (24), 6939.

Nybø, A., Nielsen, F.G., Reuder, J., et al., 2020. Evaluation of different wind fields for the investigation of the dynamic response of offshore wind turbines. Wind Energy 23 (9), 1810–1830.

Nybø, A., Gunnar Nielsen, F., Godvik, M., 2022. Sensitivity of the dynamic response of a multimegawatt floating wind turbine to the choice of turbulence model. Wind Energy 25, 1013–1029.

Nygaard, T.A., De Vaal, J., Pierella, F., et al., 2016. Development, verification and validation of 3DFloat; aero-servo-hydro-elastic computations of offshore structures. Energy Proc. 94, 425–433.

Otter, A., Murphy, J., Pakrashi, V., et al., 2022. A review of modelling techniques for floating offshore wind turbines. Wind Energy 25 (5), 831–857.

Pope, S.B., 2000. Turbulent Flows. Cambridge University Press.

Porté-Agel, F., Bastankhah, M., Shamsoddin, S., 2020. Wind-turbine and wind-farm flows: a review. Boundary-Layer Meteorol. 174 (1), 1–59.

Putri, R.M., Obhrai, C., Jakobsen, J.B., et al., 2020. Numerical analysis of the effect of offshore turbulent wind inflow on the response of a spar wind turbine. Energies 13 (10), 2506.

Robertson, A., Jonkman, J., Vorpahl, F., et al., 2014a. Offshore code comparison collaboration continuation within IEA wind task 30: phase II results regarding a floating semisubmersible wind system. F. In: Proceedings of the International Conference on Offshore Mechanics and Arctic Engineering. American Society of Mechanical Engineers.

Robertson, A., Jonkman, J., Masciola, M., et al., 2014b. Definition of the Semisubmersible Floating System for Phase II of OC4. National Renewable Energy Lab (NREL), Golden, CO (United States).

Roddier, D., Cermelli, C., Aubault, A., et al., 2010. WindFloat: a floating foundation for offshore wind turbines. J. Renew. Sustain. Energy 2 (3), 033104.

Rosen, A., Sheinman, Y., 1996. The power fluctuations of a wind turbine. J. Wind Eng. Ind. Aerod. 59 (1), 51–68.

Sebastian, T., Lackner, M., 2013. Characterization of the unsteady aerodynamics of offshore floating wind turbines. Wind Energy 16 (3), 339–352.

Skaare, B., Nielsen, F.G., Hanson, T.D., et al., 2015. Analysis of measurements and simulations from the Hywind Demo floating wind turbine. Wind Energy 18 (6), 1105–1122.

Smagorinsky, J., 1963. General circulation experiments with the primitive equations: I. The basic experiment. Mon. Weather Rev. 91 (3), 99–164.

Sorensen, J.N., Shen, W.Z., 2002. Numerical modeling of wind turbine wakes. J. Fluid Eng. 124 (2), 393–399.

Stull, R.B., 1988. An introduction to boundary layer meteorology. In: An Introduction to Boundary Layer Meteorology.

Tran, T.T., Kim, D.-H., 2016a. Fully coupled aero-hydrodynamic analysis of a semi-submersible FOWT using a dynamic fluid body interaction approach. Renew. Energy 92, 244–261.

Tran, T.T., Kim, D.H., 2016b. A CFD study into the influence of unsteady aerodynamic interference on wind turbine surge motion. Renew. Energy 90, 204–228.

Troldborg, N., Sørensen, J.N., Mikkelsen, R., 2007. Actuator line simulation of wake of wind turbine operating in turbulent inflow. In: Proceedings of the Journal of Physics: Conference Series, F. IOP Publishing.

Vermeer, L., Sørensen, J.N., Crespo, A., 2003. Wind turbine wake aerodynamics. Prog. Aero. Sci. 39 (6–7), 467–510.

Viselli, A.M., Goupee, A.J., Dagher, H.J., et al., 2016. Design and model confirmation of the intermediate scale VolturnUS floating wind turbine subjected to its extreme design conditions offshore Maine. Wind Energy 19 (6), 1161–1177.

Wang, Y., Lin, J., Duan, H., et al., 2021. Investigation on thrust characteristics of a downstream offshore floating wind turbine under yawed inflow conditions. J. Mar. Sci. Eng. 9 (11), 1215.

Xu, S., Xue, Y., Zhao, W., et al., 2022. A review of high-fidelity computational fluid dynamics for floating offshore wind turbines. J. Mar. Sci. Eng. 10 (10), 1357.

Zhang, Y., Kim, B., 2018. A fully coupled computational fluid dynamics method for analysis of semi-submersible floating offshore wind turbines under wind-wave excitation conditions based on OC5 data. Appl. Sci. 8 (11), 2314.